

Magneto-rotational instability in a solar mean-field dynamo

AXEL BRANDENBURG,^{1,2,3,4} GUSTAV LARSSON,^{1,5} FABIO DEL SORDO,^{6,7} AND PETRI J. KÄPYLÄ⁸

¹*Nordita, KTH Royal Institute of Technology and Stockholm University, Hannes Alfvéns väg 12, SE-10691 Stockholm, Sweden*

²*The Oskar Klein Centre, Department of Astronomy, Stockholm University, AlbaNova, SE-10691 Stockholm, Sweden*

³*McWilliams Center for Cosmology & Department of Physics, Carnegie Mellon University, Pittsburgh, PA 15213, USA*

⁴*School of Natural Sciences and Medicine, Ilia State University, 3-5 Cholokashvili Avenue, 0194 Tbilisi, Georgia*

⁵*Department of Physics, Stockholm University, AlbaNova, 10691 Stockholm, Sweden*

⁶*Scuola Normale Superiore, Piazza dei Cavalieri, 7 56126 Pisa, Italy*

⁷*INAF, Osservatorio Astrofisico di Catania, via Santa Sofia, 78 Catania, Italy*

⁸*Institut für Sonnenphysik (KIS), Georges-Köhler-Allee 401a, 79110 Freiburg im Breisgau, Germany*

ABSTRACT

We address the question, whether the magneto-rotational instability (MRI) can operate in the near-surface shear layer (NSSL) of the Sun and how it affects the interaction with the dynamo process. Using hydromagnetic mean-field simulations of $\alpha\Omega$ -type dynamos in rotating shearing-periodic boxes, we show that for negative shear, the MRI can operate above a certain critical shear parameter. This parameter scales inversely with the equipartition magnetic field strength above which α quenching set in. The MRI augments the usual Ω effect, but in our Cartesian cases, it is found to reduce the resulting magnetic field strength and thus suppresses the dynamo process. In view of the application to the solar NSSL, we conclude that the turbulent magnetic diffusivity may be too large for the MRI to be excited and that therefore only the standard Ω effect is expected to operate.

Keywords: Astrophysical magnetism (102) — Magnetic fields (994)

1. INTRODUCTION

The magneto-rotational instability (MRI) provides a source of turbulence in accretion discs, where it feeds upon Keplerian shear to turn potential energy into kinetic and magnetic energies; see Balbus & Hawley (1998) for a review. For the MRI to be excited, the angular velocity Ω must decrease with increasing distance ϖ from the rotation axis, i.e., $\partial\Omega/\partial\varpi < 0$. There must also be a moderately strong magnetic field. This condition is obeyed not only in accretion discs. Also in the Sun, both requirements may be satisfied in the near surface shear layer (NSSL), the outer 4% of the solar radius. This motivates the question whether the MRI might also be excited in stars like the Sun (Balbus & Hawley 1994; Urpin 1996; Masada 2011; Kagan & Wheeler 2014; Wheeler et al. 2015; Vasil et al. 2024). In addition to the Sun, the application to proto-neutron stars is a particularly prominent one (Reboul-Salze et al. 2022).

In the Sun’s outer 30% by radius, there is convection converting part of the Sun’s thermal energy into kinetic energy. Owing to the Sun’s rotation and the fact that the convection is anisotropic, the Sun’s internal angular velocity is nonuniform (Lebedinskii 1941; Wasiutynski

1946; Kippenhahn 1963; Köhler 1970; Rüdiger 1980; Brandenburg et al. 1990), causing also the emergence of the aforementioned NSSL (Rüdiger et al. 2014; Kitchatinov 2016, 2023). In addition, there are small-scale and large-scale magnetic fields as a result of the convective turbulence (Meneguzzi & Pouquet 1989; Nordlund et al. 1992; Brandenburg et al. 1996; Cattaneo 1999). The presence of radial stratification in density and/or turbulent intensity, together with global rotation, causes the occurrence of large-scale magnetic fields (Moffatt 1978; Parker 1979; Krause & Rädler 1980; Zeldovich et al. 1983). Thus, in the Sun, the two ingredients of the MRI—differential rotation and mean magnetic fields—are ultimately caused by the underlying convection.

To address the question of whether or not the MRI is excited and whether it contributes to shaping the Sun’s magnetic field to display equatorward migration of a global large-scale magnetic field, we need to separate the MRI-driven flows from the convection. One approach is to ignore convection, but to retain some of its secondary effects, i.e., the NSSL with $\partial\Omega/\partial\varpi < 0$ and magnetic fields produced by convection; see the discussion by

Vasil et al. (2024) and an appraisal by Zweibel (2024). Another approach, the one taken here, is to average over the convection. By employing azimuthal averages, one is left with a stationary, nonturbulent background. Furthermore, correlations among different components of the fluctuating parts of the turbulent velocity and magnetic fields emerge that are parameterized in terms of (i) diffusive contributions, such as turbulent viscosity and turbulent magnetic diffusion, and (ii) non-diffuse contributions such as Λ and α effects, which are chiefly responsible for producing differential rotation and large-scale magnetic fields in the Sun (Rüdiger & Hollerbach 2004). These effects explain in a self-consistent way the NSSL and the large-scale magnetic field by solving the averaged equations (Pipin 2017); see Brandenburg et al. (2023) for a review.

Using direct numerical simulations with forced turbulence, Väisälä et al. (2014) did already demonstrate that the onset of the MRI is delayed to larger magnetic Reynolds numbers by the action of turbulent diffusion, just as expected from their mean-field estimates. Averaging over the convective motions of the Sun has been done previously in the context of mean-field hydrodynamics with the Λ effect. When including compressibility and thermodynamics, it was noticed that the equations display an instability (Gierasch 1974; Schmidt 1982; Chan et al. 1987; Rüdiger & Tuominen 1991; Rüdiger & Spahn 1992), whose nature was not understood initially. However, this later turned out to be an example where averaging over the convection leads to mean-field equations that themselves are susceptible to an instability, namely the onset of convection. This depends on how close to adiabatic the mean-field state is and what the values of the turbulent viscosity and turbulent thermal diffusivities are (Tuominen et al. 1994).

When magnetic fields are present and sustained by a dynamo, the full system of magnetohydrodynamic (MHD) equations may be unstable to the MRI. We must emphasize that we are here not talking about the previously studied case where the MRI provides the source of turbulence, which then reinforces an initial magnetic field by dynamo action through a self-sustained doubly-positive feedback cycle (Brandenburg et al. 1995; Hawley et al. 1996; Stone et al. 1996). Even in that case, a mean-field description may be appropriate to quantify the nature of a large-scale dynamo governed by rotation and stratification (Brandenburg & Sokoloff 2002). However, such a description can only be an effective one, because the level of turbulence is unknown and emerges only when solving the underlying, essentially nonlinear

dynamo problem (Rincon et al. 2007; Lesur & Ogilvie 2008; Hecault et al. 2011).

In the present paper, we focus on the simpler case where a mean-field dynamo is assumed given, but potentially modified by the MRI. Ideally, in view of solar applications, it would be appropriate to consider an axisymmetric hydromagnetic mean-field dynamo with differential rotation being sustained by the Λ effect. Such systems have been studied for a long time (Brandenburg et al. 1990, 1991, 1992; Kitchatinov & Rüdiger 1995; Rempel 2006; Pipin 2017; Pipin & Kosovichev 2019), but no MRI was ever reported in such studies. One reason for this might be that it is hard to identify the operation of the MRI in a system that is already governed by a strong instability which is responsible for producing the magnetic field. We therefore take a step back and consider here a system in Cartesian geometry. In Section 2, we motivate the details of our model and present the results in Section 3. We conclude in Section 4.

2. OUR MODEL

2.1. Shearing box setup

Following the early work of Balbus & Hawley (1991, 1992) and Hawley & Balbus (1991, 1992), we study the MRI in a shearing-periodic box, where x is the cross-stream direction, y is the streamwise or azimuthal direction, and z is the spanwise or vertical direction. As in Väisälä et al. (2014), we consider the mean-field equations for azimuthally averaged velocities $\bar{\mathbf{U}}(x, z, t)$, the magnetic field $\bar{\mathbf{B}}(x, z, t)$, and the mean density $\bar{\rho}(x, z, t)$. The system is rotating with the angular velocity $\boldsymbol{\Omega}$, and there is a uniform shear flow $\bar{\mathbf{V}}(x) = (0, Sx, 0)$, so the full velocity is therefore given by $\bar{\mathbf{V}} + \bar{\mathbf{U}}$. We consider the system to be isothermal with constant sound speed c_s , so the mean pressure $\bar{p}(x, z, t)$ is given by $\bar{p} = \bar{\rho}c_s^2$. The mean magnetic field is expressed in terms of the mean magnetic vector potential $\bar{\mathbf{A}}(x, z, t)$ with $\bar{\mathbf{B}} = \nabla \times \bar{\mathbf{A}}$ to satisfy $\nabla \cdot \bar{\mathbf{B}} = 0$. The full system of equations for $\bar{\rho}$, $\bar{\mathbf{U}}$, and $\bar{\mathbf{A}}$ is given by (Brandenburg et al. 1995, 2008)

$$\frac{D \ln \bar{\rho}}{Dt} = -\nabla \cdot \bar{\mathbf{U}} \quad (1)$$

$$\begin{aligned} \frac{D \bar{\mathbf{U}}}{Dt} = & -S \bar{\mathbf{U}}_x \hat{\mathbf{y}} - 2\boldsymbol{\Omega} \times \bar{\mathbf{U}} - c_s^2 \nabla \ln \bar{\rho} \\ & + [\bar{\mathbf{J}} \times \bar{\mathbf{B}} + \nabla \cdot (2\nu_T \bar{\rho} \bar{\mathbf{S}})] / \bar{\rho}, \end{aligned} \quad (2)$$

$$\frac{\partial \bar{\mathbf{A}}}{\partial t} = -S \bar{\mathbf{A}}_y \hat{\mathbf{x}} + \bar{\mathbf{U}} \times \bar{\mathbf{B}} + \alpha \bar{\mathbf{B}} - \eta_T \mu_0 \bar{\mathbf{J}}, \quad (4)$$

where $D/Dt = \partial/\partial t + \bar{\mathbf{U}} \cdot \nabla$ is the advective derivative, $\bar{\mathbf{S}}$ is the rate-of-strain tensor of the mean flow with the

components $\bar{S}_{ij} = (\partial_i \bar{U}_j + \partial_j \bar{U}_i)/2 - \delta_{ij} \nabla \cdot \bar{U}/3$, Ω is the angular velocity, $S = -q\Omega$ is the shear parameter of the underlying flow $\bar{\mathbf{V}}(x) = (0, Sx, 0)$, and $\bar{\mathbf{J}} = \nabla \times \bar{\mathbf{B}}/\mu_0$ is the mean current density with μ_0 being the vacuum permeability. There are three mean-field parameters: the turbulent viscosity ν_T , the turbulent magnetic diffusivity η_T , and the α effect. Note that in our two-dimensional case, $\bar{\mathbf{V}} \cdot \nabla = Sx\partial_y = 0$. In some cases, we allow for α quenching and write

$$\alpha = \alpha_0 / (1 + \bar{\mathbf{B}}^2 / B_{\text{eq}}^2), \quad (5)$$

where B_{eq} is the equipartition field strength above which α begins to be affected by the feedback from the Lorentz force of the small-scale magnetic field (Ivanova & Ruzmaikin 1977). We sometimes refer to this as microphysical feedback to distinguish it from the macrophysical feedback from the Lorentz force of the large-scale magnetic field, $\bar{\mathbf{J}} \times \bar{\mathbf{B}}$. This type of saturation is sometimes also called the Malkus–Proctor mechanism, after the early paper by Malkus & Proctor (1975), who employed spherical geometry.

In the absence of α quenching ($B_{\text{eq}} \rightarrow \infty$), the only possibility for the dynamo to saturate is via the Lorentz force from the mean magnetic field, $\bar{\mathbf{J}} \times \bar{\mathbf{B}}$, i.e., the Malkus–Proctor mechanism. Also relevant to our present work is that of Schuessler (1979), who considered Cartesian geometry. Our solutions, however, are simpler still in that we employ periodic boundary conditions in most cases.

A simple way to identify the operation of the MRI in a dynamo is by comparing models with positive and negative values of q , because the MRI only works in the range $0 < q < 2$. Note also that for $q > 2$, the hydrodynamic state is Rayleigh-unstable and results in an exponentially growing shear flow, $\bar{U}_y(z)$, without ever saturating in a periodic system. In all our cases, we consider $q = \pm 3/2$.

Some of our models with $C_\Omega > 0$, where the MRI is not operating, do not saturate in the absence of α quenching. To check whether this is a peculiarity of the use of periodic boundary conditions, we also consider models with what is called a vertical field condition, i.e.,

$$\bar{B}_x = \bar{B}_y = \partial_z \bar{B}_z = 0, \quad (6)$$

which corresponds to $\partial_z \bar{A}_x = \partial_z \bar{A}_y = \bar{A}_z = 0$. Note that with this boundary condition, the normal component of the Poynting vector $\bar{\mathbf{E}} \times \bar{\mathbf{B}}/\mu_0$, where $\bar{\mathbf{E}} = \eta_T \mu_0 \bar{\mathbf{J}} - \bar{\mathbf{U}} \times \bar{\mathbf{B}}$ is the mean electric field, vanishes. Thus, energy conservation is still preserved.

2.2. Input and output parameters

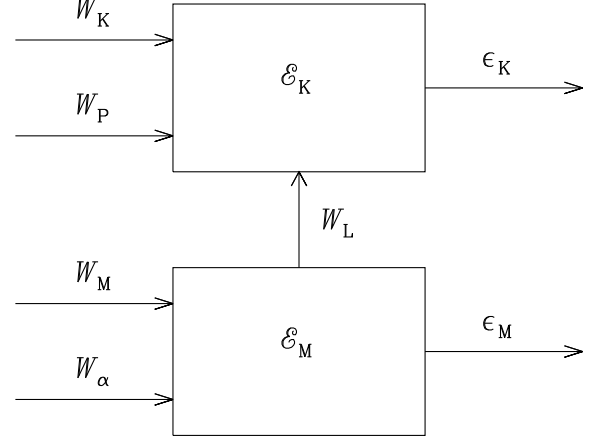


Figure 1. Flow of energy in a hydromagnetic mean-field dynamo.

We consider a two-dimensional domain $L_x \times L_z$ and define $k_1 = 2\pi/L_z$ as our reference wavenumber, which is the lowest wavenumber in the z direction. The lowest wavenumber in the x direction is $k_{1x} = 2\pi/L_x$. Our main input parameters are

$$C_\alpha = \alpha_0/\eta_T k_1, \quad C_\Omega = S/\eta_T k_1^2, \quad (7)$$

as well as $q = -S/\Omega$ and B_{eq} , which can be expressed via the corresponding Alfvén speed, $v_A^{\text{eq}} \equiv B_{\text{eq}}/\sqrt{\mu_0 \rho_0}$, in nondimensional form as

$$\mathcal{B}_{\text{eq}} \equiv v_A^{\text{eq}} k_1 / \Omega. \quad (8)$$

In all our cases, we assume $\text{Pr}_M \equiv \nu_T/\eta_T = 1$ for the turbulent magnetic Prandtl number.

Diagnostic output parameters are the energies of the mean fields that are derived either under yz or xy averaging, \mathcal{E}_M^X and \mathcal{E}_M^Z , respectively. Those are sometimes normalized by $\mathcal{E}_M^{\text{eq}} \equiv B_{\text{eq}}^2/2\mu_0$. We also monitor various parameters governing the flow of energy in our system. These include the mean kinetic and magnetic energy densities, $\mathcal{E}_K = \langle \bar{\rho} \bar{\mathbf{U}}^2/2 \rangle$ and $\mathcal{E}_M = \langle \bar{\mathbf{B}}^2/2\mu_0 \rangle$, their time derivatives, $\dot{\mathcal{E}}_K$ and $\dot{\mathcal{E}}_M$, the kinetic and magnetic energy dissipations, $\epsilon_K = \langle 2\bar{\rho} \nu_T \bar{\mathbf{S}}^2 \rangle$ and $\epsilon_M = \langle \eta_T \mu_0 \bar{\mathbf{J}}^2 \rangle$, the fluxes of kinetic and magnetic energy tapped from the shear flow, $W_K = \langle \bar{\rho} \bar{U}_x \bar{U}_y S \rangle$ and $W_M = -\langle \bar{B}_x \bar{B}_y S/\mu_0 \rangle$, the work done by the pressure force, $W_P = -\langle \bar{\mathbf{U}} \cdot \nabla \bar{p} \rangle$ as well as the work done by the α effect, $W_\alpha = \langle \alpha \bar{\mathbf{J}} \cdot \bar{\mathbf{B}} \rangle$, and the work done by the Lorentz force, $W_L = \langle \bar{\mathbf{U}} \cdot (\bar{\mathbf{J}} \times \bar{\mathbf{B}}) \rangle$. Figure 1 gives a graphical illustration showing the flow of energy in a hydromagnetic mean-field dynamo with shear.

For a uniform vertical magnetic field, $\mathbf{B}_0 = (0, 0, B_0)$, the MRI is excited when $v_{A0} k_1 < \sqrt{2\Omega S}$, where $v_{A0} =$

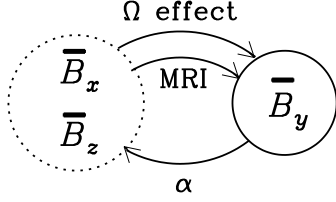


Figure 2. Sketch illustrating the generation of \overline{B}_y from \overline{B}_x through the Ω effect and from \overline{B}_z through the MRI, and the generation of both \overline{B}_x and \overline{B}_z from \overline{B}_y through the α effect.

$B_0/\sqrt{\mu_0\rho_0}$ is the Alfvén in speed of the uniform vertical magnetic field. The MRI can be modeled in one dimension with $\nabla = (0, 0, \partial_z)$. Such a one-dimensional setup could also lead to what is called an $\alpha\Omega$ dynamo, which means that the mean radial or cross-stream field \overline{B}_x is regenerated by the α effect and the mean toroidal or streamwise field \overline{B}_y is regenerated by the Ω effect or, more precisely, the shear flow $\overline{V}(x)$. One sometimes also talks about an α^2 dynamo if there is no shear, or about an $\alpha^2\Omega$ dynamo if both α effect and shear contribute to regenerating \overline{B}_y .

In the one-dimensional case with $\nabla = (0, 0, \partial_z)$ and periodic boundary conditions, the α^2 dynamo is excited when $C_\alpha > 1$, while the $\alpha\Omega$ dynamo is excited for $C_\alpha C_\Omega > 2$ (Brandenburg & Subramanian 2005). Because of $\nabla \cdot \overline{\mathbf{B}} = 0$, the resulting magnetic field is then always of the form $\overline{\mathbf{B}}(z) = (\overline{B}_x, \overline{B}_y, 0)$, i.e., $\overline{B}_z = 0$, so it is not possible to have the MRI being excited.

This would change if the dynamo also had x extent. To see this, we consider for a moment a one-dimensional domain with $\nabla = (\partial_x, 0, 0)$. In that case, an α^2 dynamo with $\overline{\mathbf{B}}(x) = (0, \overline{B}_y, \overline{B}_z)$ can be excited, allowing $\overline{B}_z \neq 0$. It would be excited when $\alpha_0/\eta_T k_{1x} \equiv C_\alpha k_1/k_{1x} > 1$, i.e., $C_\alpha > k_{1x}/k_1 = L_z/L_x$. Figure 2 gives a graphical illustration of the generation of \overline{B}_y from \overline{B}_x through the Ω effect and from \overline{B}_z through the MRI, and the generation of both \overline{B}_x and \overline{B}_z from \overline{B}_y through the α effect.

To allow for the possibility that in our two-dimensional domain such a dynamo is preferred over one with z extend, we choose our domain to be oblate, e.g., $L_x/L_z = 2$. We solve the equations with the PENCIL CODE (Pencil Code Collaboration et al. 2021) using numerical resolutions between 64×128 to 256×512 mesh points, i.e., the mesh spacings in the x and z directions are always kept the same.

2.3. Dynamo types in the Rädler diagram

It is convenient to discuss solutions in the C_α - C_Ω plane; see Figure 3. Such diagrams were extensively ex-

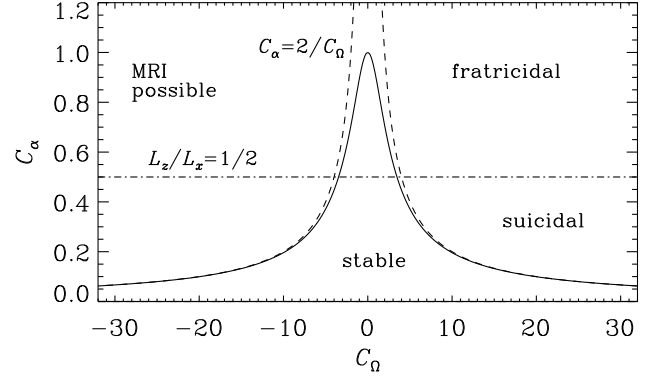


Figure 3. Rädler diagram for the $\alpha^2\Omega$ dynamo in a domain with $L_z/L_x = 1/2$. The onset location is shown as a solid line, and the pure $\alpha\Omega$ approximation ($C_\alpha C_\Omega = 2$) is shown as dashed lines.

ploited by Rädler (1986), which is why we refer to such plots in the following as Rädler diagrams. Rädler considered dynamos in spherical geometry where α changed sign about the equator, so the solutions were either symmetric or antisymmetric about the equator. In addition, they could be axisymmetric or antisymmetric and they could also be oscillatory or stationary.

For a one-dimensional $\alpha^2\Omega$ dynamo, the complex growth rate is $(\alpha^2 k^2 - i k \alpha S)^{1/2} - \eta_T k^2$. For the marginally excited state, we require the real part of the complex growth rate to vanish. This yields

$$C_\Omega = C_\alpha \sqrt{(2/C_\alpha^2 - 1)^2 - 1}, \quad (9)$$

which is the solid line shown in Figure 3.

The Rädler diagram gives a graphical overview of the differences between dynamos with positive and negative shear, i.e., positive and negative values of C_Ω . The MRI is only possible for $C_\Omega < 0$ (negative shear), while for $C_\Omega > 0$, we just expect ordinary $\alpha\Omega$ dynamo waves. This expectation, however, does not apply to dynamos in periodic domains with $\alpha_0 = \text{const}$, as was first found in the fully three-dimensional turbulence simulations of Hubbard et al. (2011). Their $\alpha\Omega$ dynamo started off as expected, but at some point during the early, nonlinear saturation phase of \mathcal{E}_M^X , the dynamo wave stopped and a new solution emerged that had a cross-stream variation, i.e., \mathcal{E}_M^X became strong and suppressed \mathcal{E}_M^Z .

A similar type of exchange of dynamo solutions in the nonlinear regime was first found by Fuchs et al. (1999) while investigating hydromagnetic dynamos with Malkus-Proctor feedback in a sphere. They found self-killing and self-creating dynamos due to the presence of different stable flow patterns where the magnetic field causes the solution to respond to a newly emerged flow pattern after the initial saturation. This was thus the

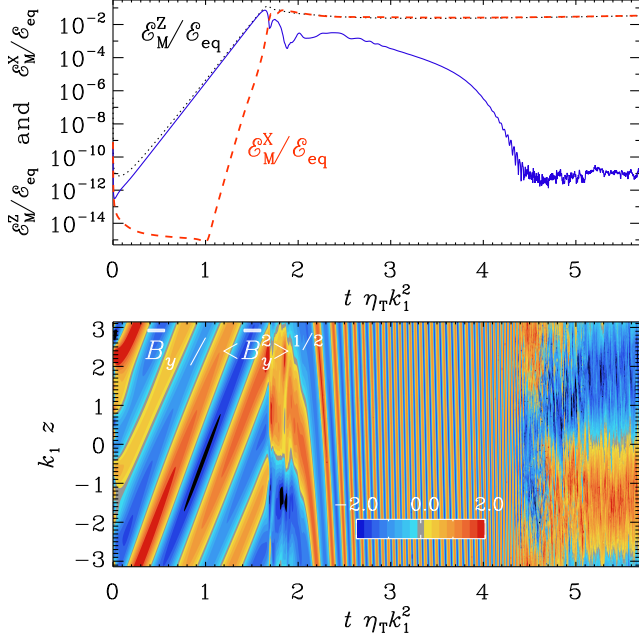


Figure 4. Time dependence of \mathcal{E}_M (dotted black line), \mathcal{E}_M^Z (solid blue line) and \mathcal{E}_M^X (dashed red line), all normalized by $\mathcal{E}_M^{\text{eq}}$, and \bar{B}_y versus t and z for a fratricidal dynamo (Run F) with $C_\alpha = 1$, $C_\Omega = 150$, $q = -3/2$ (positive shear) and $B_{\text{eq}} \rightarrow \infty$ (no α quenching). Here, \bar{B}_y has been normalized by its instantaneous rms values so as to see the dynamo wave also during the early exponential growth phase and during the late decay phase.

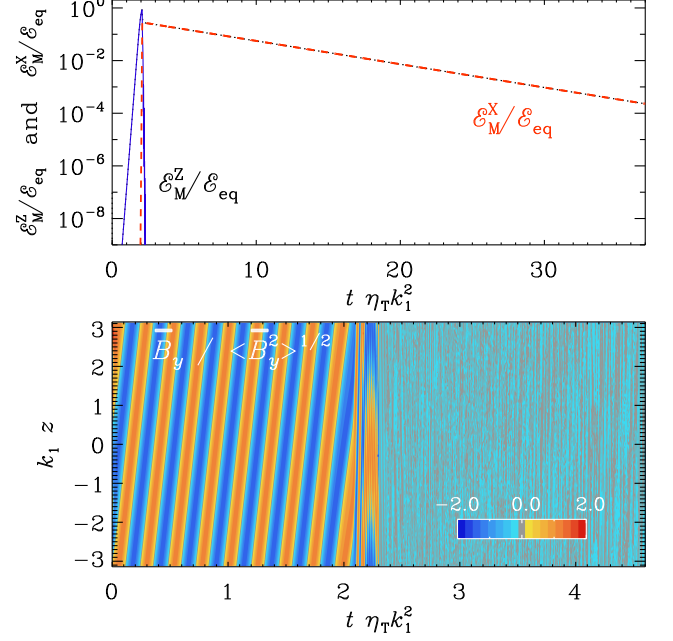


Figure 5. Similar to Figure 4, but for a suicidal dynamo with $C_\alpha = 0.49$ and $C_\Omega = 7.5$ (Run B).

first example of what then became known as a suicidal dynamo.

In analogy with the suicidal dynamos, the dynamos found by Hubbard et al. (2011) were called fratricidal dynamos. This property of dynamos in a periodic domain emerged as a problem because $\alpha\Omega$ dynamos in a periodic domain could only be studied for a limited time interval before they disappeared (Karak & Brandenburg 2016).

3. RESULTS

We begin with the discussion of fratricidal and suicidal dynamos, but emphasize that those have so far only been found in periodic systems for $C_\Omega > 0$, i.e., for positive shear. Thus, to examine the effect of the MRI, we compare solutions with positive and negative values of C_Ω using both periodic and non-periodic domains.

3.1. Fratricidal and suicidal mean-field dynamos

Here we show that fratricidal dynamos can also occur in a mean-field context. The α^2 sibling is here possible because $C_\alpha > L_z/L_x = 0.5$. This is shown in Figure 4, where we plot \mathcal{E}_M^Z and \mathcal{E}_M^X vs time, and \bar{B}_y vs t and z . In the following, this case is referred to as Run F. We

see that \mathcal{E}_M^Z grows exponentially starting from a weak seed magnetic field. The zt diagram in Figure 4 shows the usual dynamo waves. When the dynamo approaches saturation, \mathcal{E}_M^X also begins to grow exponentially, but at a rate that it is much larger than the growth rate of \mathcal{E}_M^Z . When \mathcal{E}_M^X reaches about $10^{-3}\mathcal{E}_M^{\text{eq}}$, \mathcal{E}_M^Z declines rapidly and is then overtaken by \mathcal{E}_M^X . At that moment, the dynamo waves cease and a new transient commences with a rapidly varying time dependence, but at a very low amplitude; see the zt diagram of Figure 4 for $2.5 < t\eta_T k_1^2 < 4.5$.

For $C_\alpha < 0.5$, the α^2 sibling with $\mathcal{E}_M^X \neq 0$ is impossible. Surprisingly, it turned out that the $\alpha\Omega$ dynamo can then still be killed by a secondary \mathcal{E}_M^X , but such a state with $\mathcal{E}_M^X \neq 0$ cannot be sustained and decays on an ohmic time scale; see Figure 5 for Run B. It is therefore an example of a suicidal dynamo. We see that \mathcal{E}_M^X decay towards zero, and that the dynamo wave then just disappears. By that time, \mathcal{E}_M^Z has already become very small and has disappeared within the noise.

3.2. Comparison of positive and negative shear

To identify the effect of the MRI, it is convenient to compare solutions for positive and negative shear. In Figure 6, we plot the time evolutions of \mathcal{E}_M , \mathcal{E}_M^X , and \mathcal{E}_M^Z for Runs C–G with different values of C_α and C_Ω , as well as periodic and vertical field boundary conditions. We see that, regardless of the boundary conditions, the cases with negative shear, where the MRI is possible, all

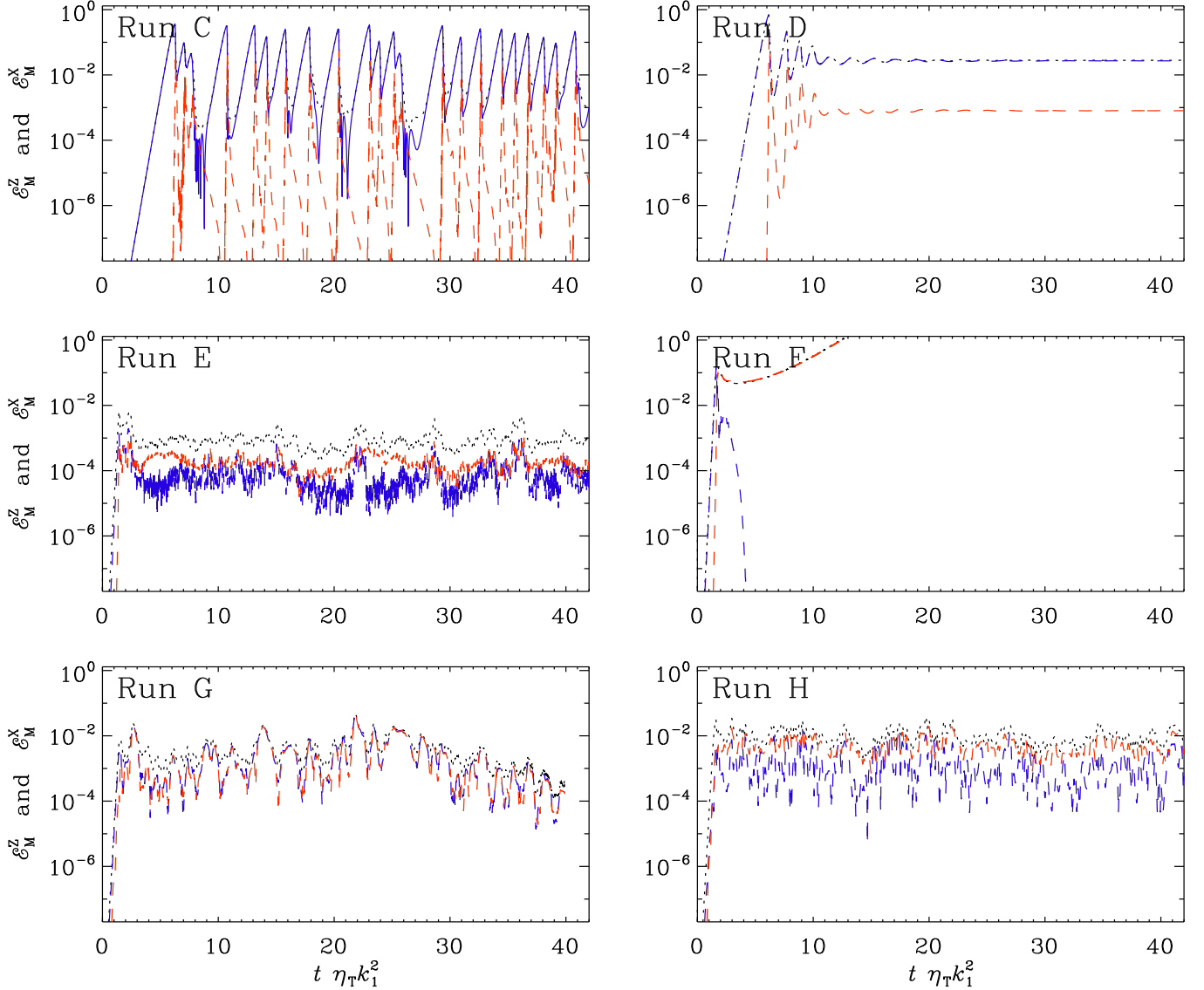


Figure 6. Comparison of solutions for $C_\Omega < 0$ (Runs C, E, and G; left panels) and $C_\Omega > 0$ (Runs D, F, and H; right panels) for periodic boundary conditions (top) and vertical field boundary conditions (bottom). As in the upper panels of Figures 4 and 5, \mathcal{E}_M (dotted black line), \mathcal{E}_M^Z (solid blue line), and \mathcal{E}_M^X (dashed red line), normalized by $\mathcal{E}_M^{\text{eq}}$, are shown versus t .

have less magnetic energy than the cases with positive shear. Thus, the action of the MRI always diminishes dynamo action.

Various parameters related to the flow of energy are summarized in Table 1. We see that W_L is always positive, i.e., magnetic energy goes into kinetic energy. But we also see that whenever C_Ω is negative and the MRI is excited, W_L and ϵ_M are always much larger than for positive values of C_Ω , when the MRI does not operate. It is remarkable that in the latter case, when only the standard Ω effect operates, W_K is often even negative. Note also that W_P is not being given, because its value is very small. Likewise, $\dot{\mathcal{E}}_M$ and $\dot{\mathcal{E}}_K$ are small and not listed, but are still included in the calculation of the

total

$$\text{gain} = W_M + W_K + W_\alpha + W_P \quad (10)$$

and

$$\text{loss} = \epsilon_M + \epsilon_K + \dot{\mathcal{E}}_M + \dot{\mathcal{E}}_K. \quad (11)$$

Both the total gain and the total loss balance each other nearly perfectly.

Interestingly, the ratio ϵ_K/ϵ_M , which is known to scale with the microphysical magnetic Prandtl number in direct numerical simulations of forced turbulence (Brandenburg 2014), varies widely in the present mean-field calculations. It is always less than unity, and often much less than unity. On the other hand, not much is known about the scaling of this dissipation ra-

Table 1. Summary of the runs. The column BC gives 0 (1) for periodic (vertical field) boundary conditions. For runs without α quenching we have $\mathcal{B}_{\text{eq}}^{-1} = 0$. \mathcal{E}_{M} and \mathcal{E}_{K} are given in units of $\rho_0 \Omega^2 / k_1^2$. The energy fluxes W_{M} , W_{K} , W_{α} , W_{L} , ϵ_{M} , ϵ_{K} , as well as gain and losses are in units of $\eta_{\text{T}} k_1^2 \mathcal{E}_{\text{M}}$.

Run	BC	$\mathcal{B}_{\text{eq}}^{-1}$	C_{α}	C_{Ω}	\mathcal{E}_{M}	\mathcal{E}_{K}	W_{M}	W_{K}	W_{α}	W_{L}	ϵ_{M}	ϵ_{K}	gain	loss
A	0	0	0.49	-7.5	6.45	0.83	2.4	0.280	0.480	0.13	2.8	0.41	3.2	3.2
B	0	0	0.49	7.5	2.25	4.35	0.0	-0.000	0.490	0.00	0.5	0.00	0.5	0.5
C	0	0	0.20	-15	4.48	0.18	2.3	0.064	0.085	0.03	2.4	0.10	2.5	2.5
D	0	0	0.20	15	1.40	0.04	2.0	-0.001	0.080	0.04	2.0	0.04	2.0	2.1
E	0	0	1.00	-150	0.08	0.55	39.0	10.000	2.000	6.00	35.0	16.00	51.0	51.0
F	0	0	1.00	150	2.83	1.52	0.3	0.002	1.700	0.40	1.9	0.36	2.1	2.2
G	1	0	1.00	-150	0.40	0.64	20.0	5.600	1.300	2.00	20.0	6.60	27.0	27.0
H	1	0	1.00	150	0.55	0.49	8.8	-0.340	0.780	3.50	6.6	3.10	9.2	9.7
I	0	1	0.49	-7.5	0.34	0.00	1.8	0.000	0.170	0.00	2.0	0.00	2.0	2.0
J	0	1	0.49	-30	2.41	0.00	2.0	-0.000	0.028	0.00	2.0	0.00	2.0	2.0
K	0	1	0.49	-75	0.10	0.50	11.0	0.980	0.250	2.80	8.0	4.00	12.0	12.0
L	0	1	0.49	-150	0.09	0.38	17.0	1.400	0.280	2.90	14.0	4.30	19.0	19.0
M	0	1	0.49	-300	0.04	0.51	31.0	3.400	0.330	8.20	23.0	12.00	35.0	35.0
N	0	10	0.49	-30	0.02	0.00	2.0	-0.000	0.027	0.00	2.0	0.00	2.0	2.0
O	0	10	0.49	-75	0.07	0.00	2.0	-0.000	0.008	0.00	2.0	0.00	2.0	2.0
P	0	10	0.49	-300	0.28	0.00	2.1	-0.000	0.001	0.00	2.1	0.00	2.1	2.1
Q	0	10	0.49	-750	0.22	0.01	3.9	-0.000	0.010	0.04	3.9	0.04	4.0	3.9
R	0	10	0.49	-1500	0.19	0.02	6.6	0.008	0.003	0.10	7.6	0.12	6.6	6.6
S	0	10	0.49	-3000	0.08	0.01	16.0	0.900	0.021	-0.11	16.0	0.86	17.0	19.0
T	0	100	0.49	-300	0.00	0.00	2.1	-0.000	0.002	0.00	2.1	0.00	2.1	2.1
U	0	100	0.49	-750	0.01	0.00	2.1	-0.000	0.000	0.00	2.1	0.00	2.1	2.1
V	0	100	0.49	-1500	0.01	0.00	2.1	-0.000	0.000	0.00	2.1	0.00	2.1	2.1
W	0	100	0.49	-3000	0.02	0.00	2.5	-0.000	0.000	0.00	2.3	0.00	2.5	2.5
X	0	100	0.49	-7500	0.02	0.00	4.3	0.000	0.000	0.01	3.4	0.01	4.3	4.3
Y	0	100	0.49	-15000	0.01	0.00	13.0	0.000	0.000	0.01	9.8	0.00	13.0	13.0

394 tio for MRI-driven turbulence. In the old simulations
 395 of Brandenburg et al. (1995), this ratio was found to be
 396 even slightly larger than unity. Given that we present
 397 only a coarse coverage of a fairly large parameter space
 398 in the Rädler diagram, it is possible that there are some
 399 relationships that cannot presently be discerned.

3.3. Magnetic field structures

401 It is instructive to inspect the magnetic field struc-
 402 tures of individual snapshots. This is shown in Figure 7,
 403 where we present visualizations of field lines in the xz
 404 plane together with a color scale representation of \bar{B}_y
 405 for Runs C–H. In our two dimensional case, field lines
 406 are shown as contour of \bar{A}_y . Runs C and D have a
 407 predominantly vertical dependence, which was already
 408 indicated by the dominance of \mathcal{E}_{M}^Z over \mathcal{E}_{M}^X in Figure 6.
 409 As we have seen before, the MRI is operating in Run C,
 410 and this causes some residual x dependence in the field,
 411 as manifested by the wavy pattern.

412 Run F is the complete opposite of Run D, because now
 413 there is only a pure x dependence. Again, this was also
 414 already indicated in Figure 6 through the dominance of
 415 \mathcal{E}_{M}^X over \mathcal{E}_{M}^Z . This dramatic difference is explained by
 416 the value of $C_{\alpha} = 1$, which is now large enough for an
 417 α^2 dynamo with x extend to be excited.

418 Runs E and G show predominantly small-scale struc-
 419 tures. There is no strong difference between the periodic
 420 and nonperiodic runs, except that the field lines are now
 421 purely vertical on the boundaries. It is these small-scale
 422 structures that are responsible for the enhanced dissipa-
 423 tion and ultimately for the decreased efficiency of the
 424 dynamo process in the presence of the MRI.

425 Also Run H also has small-scale structures, but those
 426 are not related to the MRI, which is absent in this run
 427 with positive shear. Here, the existence of small-scale
 428 structures is probably related to presence of boundaries
 429 in the z direction. They lower the excitation conditions
 430 for dynamo action with magnetic field dependence in

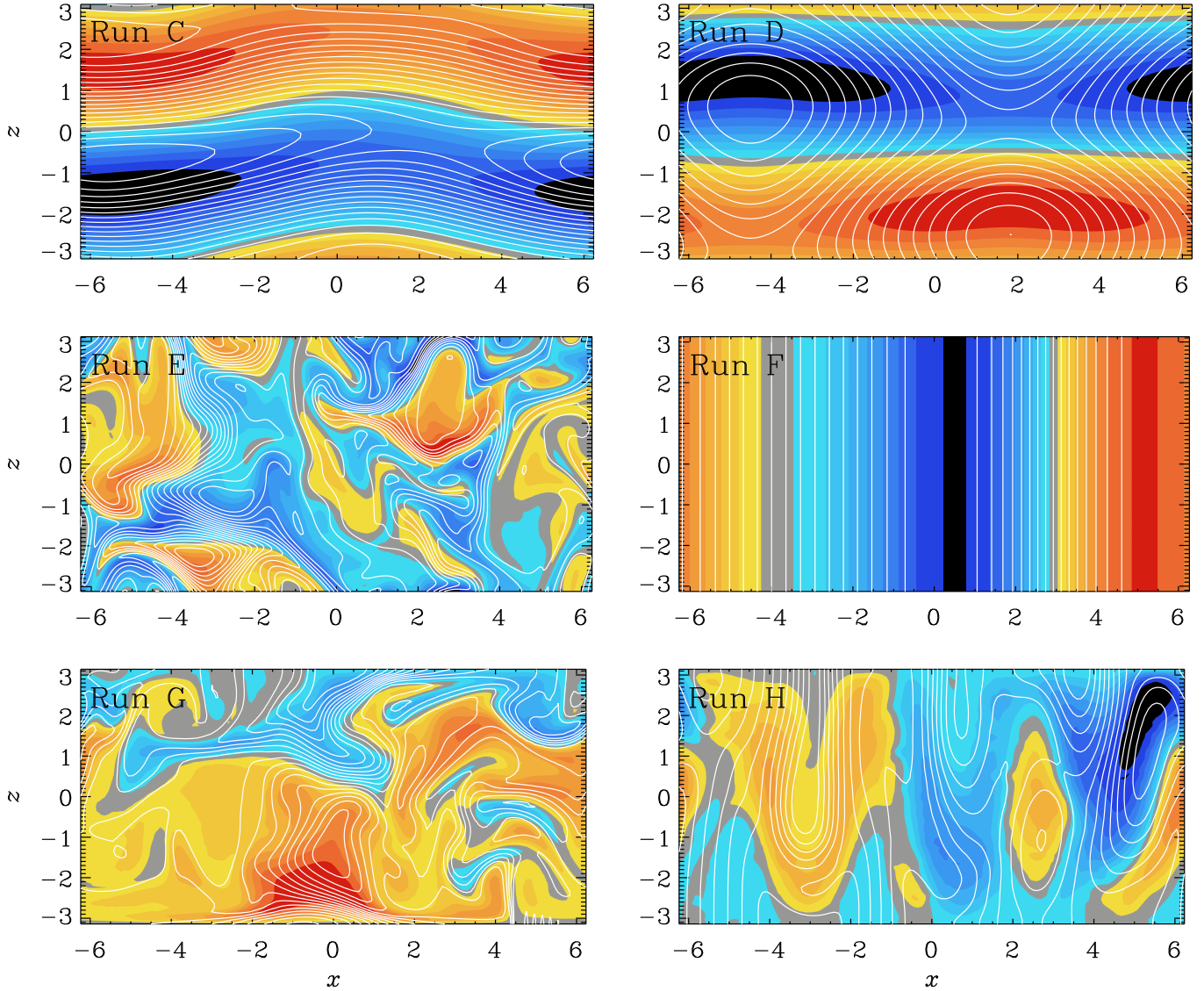


Figure 7. Visualizations of field lines of $(\overline{B}_x, \overline{B}_z)$ in the xz plane on top of a color scale representation of \overline{B}_y for Runs C–H, where blue (red) shades refer to negative (positive) values.

the z direction, but there could also be other reasons for the existence of small-scale structures in this case.

3.4. Simulations with vertical boundary conditions

Next, we study the mean magnetic field evolution for simulations with vertical field boundary conditions in the z direction. The resulting zt diagrams are shown in Figure 8 for $C_\Omega = -150$ and $+150$ using $C_\alpha = 1$. Note that during the early kinematic phase, there is clear evidence for dynamo waves migrating in the negative (positive) z direction for negative (positive) values of C_Ω .

Comparing Runs F and G in Table 1, they have the same parameters, but Run G has vertical field boundary conditions. We see that W_K is much larger in Run G than in Run F. Also W_L is significantly larger in Run G,

but the difference is here not quite as large. This is presumably caused by the existence of small-scale structures in Run G, while Run F has essentially only a one-dimensional field structure at late times.

3.5. Transition from Ω effect to MRI

When C_Ω is small enough, the turbulent magnetic diffusivity may be too large for the MRI to be excited. This idea assumes that the magnetic field is held fixed, but this is not true when the magnetic field is still being amplified by dynamo action and saturation by the large-scale Lorentz force has not yet been achieved. Therefore, it is not surprising if the MRI can occur even for small values of C_Ω .

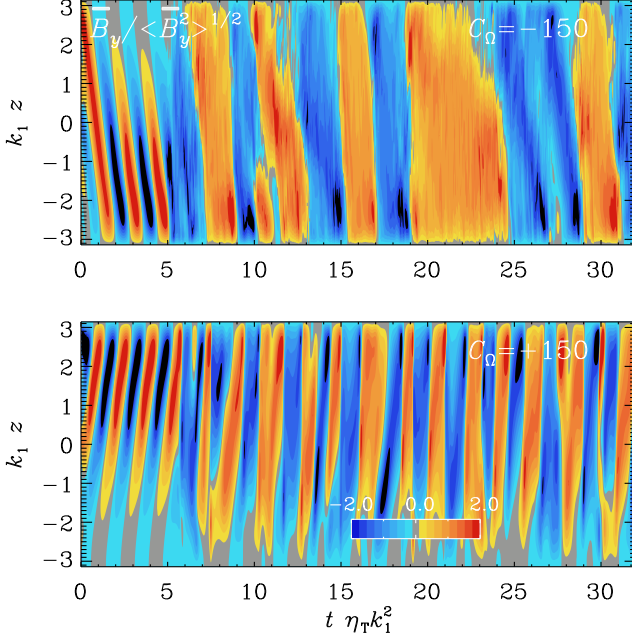


Figure 8. Mean magnetic field evolution in a z t diagram for simulations with vertical field boundary conditions in the z direction for $C_\Omega = -150$ (upper panel) and $C_\Omega = +150$ (lower panel) using $C_\alpha = 0.2$.

To facilitate dynamo saturation at a lower magnetic field strength, and therefore a regime with $C_\Omega < 0$ without MRI, we now invoke α quenching with finite values of B_{eq} . (The case without α quenching corresponds to $B_{\text{eq}} \rightarrow \infty$.) We have performed numerical experiments for different values of B_{eq} and C_Ω . It turns out that for a fixed value of B_{eq} , there is a critical value of C_Ω above which the MRI commences. This is shown in Figure 9, where we plot the mean magnetic energy density versus $-C_\Omega$ (for $C_\Omega < 0$) and a fixed value of $C_\alpha = 0.49$. We see that \mathcal{E}_M increases approximately linearly with $|C_\Omega|$ and has the same value when normalized by the respective value of $\mathcal{E}_M^{\text{eq}}$. Because the normalized values $\mathcal{E}_M/\mathcal{E}_M^{\text{eq}}$ are the same for different values of $|C_\Omega|$ and different values of \mathcal{E}_M , this saturation dependence is a consequence of α quenching. Above a certain value of $|C_\Omega|$, however, the increasing trend stops and \mathcal{E}_M begins to decline with increasing values of $|C_\Omega|$. We associate this with the onset of the MRI.

The MRI onset occurs for smaller values of $|C_\Omega|$ when B_{eq} is large. This is understandable, because for large values of B_{eq} , α quenching commences only for stronger magnetic fields. Therefore, magnetic field saturation can be accomplished by the MRI before α quenching would be able to act. From the inset of Figure 9, we find quantitatively

$$C_\Omega^{\text{crit}} \approx 30 B_{\text{eq}}^{-1}. \quad (12)$$

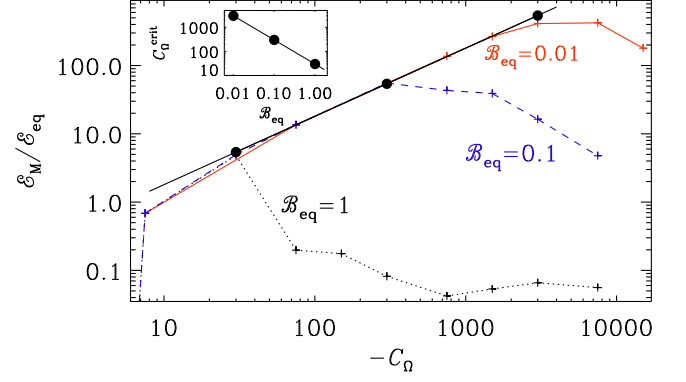


Figure 9. Dependence of $\mathcal{E}_M/\mathcal{E}_M^{\text{eq}}$ on C_Ω for $B_{\text{eq}} = 1$ (black dotted line), 0.1 (blue dashed line), and 0.01 (red solid line) using $C_\alpha = 0.49$ in all cases. The black solid line denotes $\mathcal{E}_M/\mathcal{E}_M^{\text{eq}} = 0.18 |C_\Omega|$ and the filled circles on this line denote the approximate values where \mathcal{E}_M departs from the linearly increasing trend with $|C_\Omega|$. The inset shows the dependence of C_Ω^{crit} vs $v_A^{\text{eq}} k_1 / \Omega$.

Thus, although $C_\Omega < 0$, the standard Ω effect is expected to operate in the range

$$2/C_\alpha \lesssim |C_\Omega| \lesssim C_\Omega^{\text{crit}}, \quad (13)$$

and the MRI is only possible for larger values of $|C_\Omega|$.

3.6. Comparison with earlier work

Let us now discuss whether the MRI might have been excited in previously published work. Hydro-magnetic models with α and Λ effects were considered by Brandenburg et al. (1992) using spherical geometry. The sign of C_Ω was determined by the sign of the Λ effect. Their C_Ω is defined based on the stellar radius R and can therefore not directly be compared with the C_Ω used in the present work. Also, given that the differential rotation emerges as a result of the Λ effect and is already affected by the magnetic field, their C_Ω is an output parameter.

In their Run T5 of model A−, they found $C_\Omega = -474$, while for their Run T7 of model A+, they found $C_\Omega = +939... + 1010$. The magnetic field in this model was oscillatory, which explains the existence of a range of C_Ω .

To address the question whether the MRI operated in their model A−, we can look at the resulting magnetic field strengths and compare them with model A+. They specified the decadic logarithms and found a magnetic energy of $\mathcal{E}_M = 10^{4.03}$ for their model A− and $\mathcal{E}_M = 10^{3.77...3.90}$ for their model A+. If the MRI was operational, we might have expected that \mathcal{E}_M would be suppressed in their model A− relative to their model A+, but the opposite is the case. The fact that $|C_\Omega|$ was

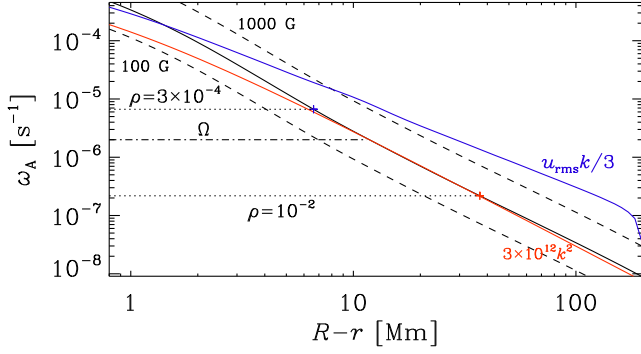


Figure 10. Depth dependence of the Alfvén frequency for $B_{\text{rms}} = 300$ G (solid black line) using the mixing length model of Spruit (1974). Also shown are the values for $B_{\text{rms}} = 1000$ G and $B_{\text{rms}} = 100$ G (upper and lower dashed lines), as well as $u_{\text{rms}}k/3$ (blue) and $3 \times 10^{12} \text{ cm}^2 \text{ s}^{-1} k^2$ (red line).

smaller in their Run T5 compared to Run T7 makes the difference even larger, because a smaller $|C_\Omega|$ should have resulted in an even weaker magnetic field.

To decide about the excitation of the MRI, we can also estimate their effective value of $v_A k_1 / \Omega$. Using $v_A \approx \sqrt{2\mathcal{E}_M / \rho_0} \approx 150$, $k_1 = 2\pi / 0.3R \approx 20$, $\Omega = \text{Ta}^{1/2} \eta_T / 2R^2 \approx 2700$, where $\text{Ta} = 3 \times 10^7$ is the turbulent Taylor number, and $\text{Pr}_M = 1$, we find $v_A k_1 / \Omega \approx 1$, so the MRI might well have been excited.

Similar conclusions about the lack of a suppression for $C_\Omega < 0$ can also be drawn from the models of Brandenburg et al. (1991) when $\text{Ta} \geq 10^6$, but for $\text{Ta} \leq 10^4$, they did find a suppression of \mathcal{E}_M for $C_\Omega < 0$.

3.7. Estimates for the Sun

For the MRI to be excited, the Alfvén frequency, $\omega_A = v_A k$, must not exceed the rotational shear frequency, $\sqrt{2q}\Omega$, where $q = -\partial \ln \Omega / \partial \ln \varpi$ is the local nondimensional shear parameter. Here, we estimate $k \approx 1/\ell$, where ℓ is the local mixing length, which is also approximately equal to the depth, $R - r$, where R is the solar radius and r is the local radius. In Figure 10, we plot the depth dependence of ω_A on $R - r$, where the radial dependence of ℓ and ρ has been obtained from the solar mixing length model of Spruit (1974). Here, we also present two estimates of the turbulent magnetic diffusion rate $\eta_T k^2$, where we assume either a constant η_T ($3 \times 10^{12} \text{ cm}^2 \text{ s}^{-1}$) or $\eta_T = u_{\text{rms}} / 3k$ (Sur et al. 2008). Both show a similar dependence on depth.

Using for the Sun $B_{\text{rms}} = 300$ G, we have $v_A = 50 \text{ m s}^{-1}$ and $\omega_A = 7 \times 10^{-6} \text{ s}^{-1}$ at a depth of 7 Mm where $\rho \approx 3 \times 10^{-4} \text{ g cm}^{-3}$, and $v_A = 8 \text{ m s}^{-1}$ and $\omega_A = 2 \times 10^{-7} \text{ s}^{-1}$ at a depth of 40 Mm where $\rho \approx 10^{-2} \text{ g cm}^{-3}$. These value bracket the value of Ω , so the MRI might be viable somewhere in this range. However, different esti-

mates for the turbulent diffusion time, $u_{\text{rms}}k/3$ (shown in blue) and $3 \times 10^{12} \text{ cm}^2 \text{ s}^{-1} k^2$ (shown in red) lie clearly above ω_A at all depth, making the MRI impossible to excite.

4. CONCLUSIONS

The MRI can only work when $C_\Omega < 0$. Our work has shown that in that case, the magnetic energy is smaller than for $C_\Omega > 0$, although all other conditions are comparable. This indicates that in those simulation the MRI does operate. Our conclusions regarding earlier findings in spherical domains remain inconclusive. The models of Brandenburg et al. (1991, 1992), where the MRI is potentially excited, show different results for a slow and rapid rotation. Therefore, it still needs to be examined whether the MRI was indeed operating in those early investigations. Alternatively, it is possible that models with positive and negative values of C_Ω are not so straightforwardly comparable as in our present Cartesian geometry.

Even in the absence of the MRI, the cases with positive and negative values of C_Ω may not be comparable. Looking at Rädler diagrams for dynamos in spheres (see also Brandenburg et al. 1989), we see significant differences in the type of solutions that are being excited and in their critical values of C_α for positive and negative values of C_Ω .

Our work has also shown that the MRI can work even for small shear parameters. A possible way to prevent the MRI from occurring is by invoking α quenching. This would then limit the magnetic field strength, which could then drop below the critical value above which magnetically diffusive effects no longer limit the MRI.

This research was supported in part by the Swedish Research Council (Vetenskapsrådet) under Grant No. 2019-04234, the National Science Foundation under Grants No. NSF PHY-2309135, AST-2307698, and NASA Awards 80NSSC22K0825 and 80NSSC22K1265. We acknowledge the allocation of computing resources provided by the Swedish National Allocations Committee at the Center for Parallel Computers at the Royal Institute of Technology in Stockholm.

Software and Data Availability. The source code used for the simulations of this study, the PENCIL CODE (Pencil Code Collaboration et al. 2021), is freely available on <https://github.com/pencil-code>. The simulation setups and corresponding input and reduced output data are freely available on <http://norlx65.nordita.org/~brandenb/projects/Solar-MRI>.

REFERENCES

- Balbus, S. A., & Hawley, J. F. 1991, *ApJ*, 376, 214, doi: [10.1086/170270](https://doi.org/10.1086/170270)
- . 1992, *ApJ*, 400, 610, doi: [10.1086/172022](https://doi.org/10.1086/172022)
- . 1994, *MNRAS*, 266, 769, doi: [10.1093/mnras/266.4.769](https://doi.org/10.1093/mnras/266.4.769)
- . 1998, *RvMP*, 70, 1, doi: [10.1103/RevModPhys.70.1](https://doi.org/10.1103/RevModPhys.70.1)
- Brandenburg, A. 2014, *ApJ*, 791, 12, doi: [10.1088/0004-637X/791/1/12](https://doi.org/10.1088/0004-637X/791/1/12)
- Brandenburg, A., Elstner, D., Masada, Y., & Pipin, V. 2023, *SSR*, 219, 55, doi: [10.1007/s11214-023-00999-3](https://doi.org/10.1007/s11214-023-00999-3)
- Brandenburg, A., Jennings, R. L., Nordlund, Å., et al. 1996, *JFM*, 306, 325, doi: [10.1017/S0022112096001322](https://doi.org/10.1017/S0022112096001322)
- Brandenburg, A., Krause, F., Meinel, R., Moss, D., & Tuominen, I. 1989, *A&A*, 213, 411
- Brandenburg, A., Moss, D., Rüdiger, G., & Tuominen, I. 1991, *GApFD*, 61, 179, doi: [10.1080/03091929108229043](https://doi.org/10.1080/03091929108229043)
- Brandenburg, A., Moss, D., & Tuominen, I. 1992, *A&A*, 265, 328
- Brandenburg, A., Nordlund, A., Stein, R. F., & Torkelsson, U. 1995, *ApJ*, 446, 741, doi: [10.1086/175831](https://doi.org/10.1086/175831)
- Brandenburg, A., Rädler, K.-H., Rheinhardt, M., & Käpylä, P. J. 2008, *ApJ*, 676, 740, doi: [10.1086/527373](https://doi.org/10.1086/527373)
- Brandenburg, A., & Sokoloff, D. 2002, *GApFD*, 96, 319, doi: [10.1080/03091920290032974](https://doi.org/10.1080/03091920290032974)
- Brandenburg, A., & Subramanian, K. 2005, *PhRep*, 417, 1, doi: [10.1016/j.physrep.2005.06.005](https://doi.org/10.1016/j.physrep.2005.06.005)
- Brandenburg, A., Tuominen, I., Moss, D., & Rüdiger, G. 1990, *Sol. Phys.*, 128, 243, doi: [10.1007/BF00154160](https://doi.org/10.1007/BF00154160)
- Cattaneo, F. 1999, *ApJL*, 515, L39, doi: [10.1086/311962](https://doi.org/10.1086/311962)
- Chan, K. L., Sofia, S., & Mayr, H. G. 1987, in *The Internal Solar Angular Velocity*, ed. B. R. Durney & S. Sofia, Vol. 137, 347, doi: [10.1007/978-94-009-3903-5_35](https://doi.org/10.1007/978-94-009-3903-5_35)
- Fuchs, H., Rädler, K. H., & Rheinhardt, M. 1999, *AN*, 320, 129, doi: [10.1002/1521-3994\(199907\)320:3\(129::AID-ASNA129\)3.0.CO;2-W](https://doi.org/10.1002/1521-3994(199907)320:3(129::AID-ASNA129)3.0.CO;2-W)
- Gierasch, P. J. 1974, *ApJ*, 190, 199, doi: [10.1086/152864](https://doi.org/10.1086/152864)
- Hawley, J. F., & Balbus, S. A. 1991, *ApJ*, 376, 223, doi: [10.1086/170271](https://doi.org/10.1086/170271)
- . 1992, *ApJ*, 400, 595, doi: [10.1086/172021](https://doi.org/10.1086/172021)
- Hawley, J. F., Gammie, C. F., & Balbus, S. A. 1996, *ApJ*, 464, 690, doi: [10.1086/177356](https://doi.org/10.1086/177356)
- Herault, J., Rincon, F., Cossu, C., et al. 2011, *PhRvE*, 84, 036321, doi: [10.1103/PhysRevE.84.036321](https://doi.org/10.1103/PhysRevE.84.036321)
- Hubbard, A., Rheinhardt, M., & Brandenburg, A. 2011, *A&A*, 535, A48, doi: [10.1051/0004-6361/201116705](https://doi.org/10.1051/0004-6361/201116705)
- Ivanova, T. S., & Ruzmaikin, A. A. 1977, *SvA*, 21, 479
- Kagan, D., & Wheeler, J. C. 2014, *ApJ*, 787, 21, doi: [10.1088/0004-637X/787/1/21](https://doi.org/10.1088/0004-637X/787/1/21)
- Karak, B. B., & Brandenburg, A. 2016, *ApJ*, 816, 28, doi: [10.3847/0004-637X/816/1/28](https://doi.org/10.3847/0004-637X/816/1/28)
- Kippenhahn, R. 1963, *ApJ*, 137, 664, doi: [10.1086/147539](https://doi.org/10.1086/147539)
- Kitchatinov, L. L. 2016, *AstL*, 42, 339, doi: [10.1134/S1063773716050054](https://doi.org/10.1134/S1063773716050054)
- . 2023, *AstL*, 49, 754, doi: [10.1134/S106377372311004X](https://doi.org/10.1134/S106377372311004X)
- Kitchatinov, L. L., & Rüdiger, G. 1995, *A&A*, 299, 446
- Köhler, H. 1970, *Sol. Phys.*, 13, 3, doi: [10.1007/BF00963937](https://doi.org/10.1007/BF00963937)
- Krause, F., & Rädler, K.-H. 1980, *Mean-Field Magnetohydrodynamics and Dynamo Theory* (Oxford: Pergamon Press)
- Lebedinskii, A. I. 1941, *Astron. Zh.*, 18, 10
- Lesur, G., & Ogilvie, G. I. 2008, *A&A*, 488, 451, doi: [10.1051/0004-6361:200810152](https://doi.org/10.1051/0004-6361:200810152)
- Malkus, W. V. R., & Proctor, M. R. E. 1975, *JFM*, 67, 417, doi: [10.1017/S0022112075000390](https://doi.org/10.1017/S0022112075000390)
- Masada, Y. 2011, *MNRAS*, 411, L26, doi: [10.1111/j.1745-3933.2010.00987.x](https://doi.org/10.1111/j.1745-3933.2010.00987.x)
- Meneguzzi, M., & Pouquet, A. 1989, *JFM*, 205, 297, doi: [10.1017/S0022112089002041](https://doi.org/10.1017/S0022112089002041)
- Moffatt, H. K. 1978, *Magnetic Field Generation in Electrically Conducting Fluids* (Cambridge: Cambridge University Press)
- Nordlund, A., Brandenburg, A., Jennings, R. L., et al. 1992, *ApJ*, 392, 647, doi: [10.1086/171465](https://doi.org/10.1086/171465)
- Parker, E. N. 1979, *Cosmical Magnetic Fields: Their Origin and Their Activity* (Oxford: Clarendon Press)
- Pencil Code Collaboration, Brandenburg, A., Johansen, A., et al. 2021, *J. Open Source Software*, 6, 2807, doi: [10.21105/joss.02807](https://doi.org/10.21105/joss.02807)
- Pipin, V. V. 2017, *MNRAS*, 466, 3007, doi: [10.1093/mnras/stw3182](https://doi.org/10.1093/mnras/stw3182)
- Pipin, V. V., & Kosovichev, A. G. 2019, *ApJ*, 887, 215, doi: [10.3847/1538-4357/ab5952](https://doi.org/10.3847/1538-4357/ab5952)
- Rädler, K. H. 1986, *AN*, 307, 89, doi: [10.1002/asna.2113070205](https://doi.org/10.1002/asna.2113070205)
- Reboul-Salze, A., Guilet, J., Raynaud, R., & Bugli, M. 2022, *A&A*, 667, A94, doi: [10.1051/0004-6361/202142368](https://doi.org/10.1051/0004-6361/202142368)
- Rempel, M. 2006, *ApJ*, 647, 662, doi: [10.1086/505170](https://doi.org/10.1086/505170)
- Rincon, F., Ogilvie, G. I., & Proctor, M. R. E. 2007, *PhRvL*, 98, 254502, doi: [10.1103/PhysRevLett.98.254502](https://doi.org/10.1103/PhysRevLett.98.254502)
- Rüdiger, G. 1980, *GApFD*, 16, 239, doi: [10.1080/03091928008243659](https://doi.org/10.1080/03091928008243659)
- Rüdiger, G., & Hollerbach, R. 2004, *The magnetic universe: geophysical and astrophysical dynamo theory* (Weinheim: Wiley)
- Rüdiger, G., Küker, M., & Tereshin, I. 2014, *A&A*, 572, L7, doi: [10.1051/0004-6361/201424953](https://doi.org/10.1051/0004-6361/201424953)
- Rüdiger, G., & Spahn, F. 1992, *Sol. Phys.*, 138, 1, doi: [10.1007/BF00146192](https://doi.org/10.1007/BF00146192)

- 695 Rüdiger, G., & Tuominen, I. 1991, in IAU Colloq. 130: The
 696 Sun and Cool Stars. Activity, Magnetism, Dynamos, ed.
 697 I. Tuominen, D. Moss, & G. Rüdiger, Vol. 380
 698 (Heidelberg: Springer), 172,
 699 doi: [10.1007/3-540-53955-7_123](https://doi.org/10.1007/3-540-53955-7_123)
 700 Schmidt, W. 1982, GApFD, 21, 27,
 701 doi: [10.1080/03091928208209004](https://doi.org/10.1080/03091928208209004)
 702 Schuessler, M. 1979, A&A, 72, 348
 703 Spruit, H. C. 1974, SoPh, 34, 277, doi: [10.1007/BF00153665](https://doi.org/10.1007/BF00153665)
 704 Stone, J. M., Hawley, J. F., Gammie, C. F., & Balbus,
 705 S. A. 1996, ApJ, 463, 656, doi: [10.1086/177280](https://doi.org/10.1086/177280)
 706 Sur, S., Brandenburg, A., & Subramanian, K. 2008,
 707 MNRAS, 385, L15, doi: [10.1111/j.1745-3933.2008.00423.x](https://doi.org/10.1111/j.1745-3933.2008.00423.x)
 708 Tuominen, I., Brandenburg, A., Moss, D., & Rieutord, M.
 709 1994, A&A, 284, 259
 710 Urpin, V. A. 1996, MNRAS, 280, 149,
 711 doi: [10.1093/mnras/280.1.149](https://doi.org/10.1093/mnras/280.1.149)
 712 Väisälä, M. S., Brandenburg, A., Mitra, D., Käpylä, P. J.,
 713 & Mantere, M. J. 2014, A&A, 567, A139,
 714 doi: [10.1051/0004-6361/201322837](https://doi.org/10.1051/0004-6361/201322837)
 715 Vasil, G. M., Lecoanet, D., Augustson, K., et al. 2024,
 716 Natur, 629, 769, doi: [10.1038/s41586-024-07315-1](https://doi.org/10.1038/s41586-024-07315-1)
 717 Wasiutynski, J. 1946, Astrophysica Norvegica, 4, 1
 718 Wheeler, J. C., Kagan, D., & Chatzopoulos, E. 2015, ApJ,
 719 799, 85, doi: [10.1088/0004-637X/799/1/85](https://doi.org/10.1088/0004-637X/799/1/85)
 720 Zeldovich, Ya. B., Ruzmaikin, A. A., & Sokoloff, D. D.
 721 1983, Magnetic Fields in Astrophysics (New York:
 722 Gordon and Breach)
 723 Zweibel, E. 2024, Natur, 629, 762,
 724 doi: [10.1038/d41586-024-01357-1](https://doi.org/10.1038/d41586-024-01357-1)